PRECEDING PAGE BLANK NOT FILMED

N92-27467

Viscous Three–Dimensional Calculations of Transonic Fan Performance

Dr. Rodrick V. Chima
NASA Lewis Research Center
Cleveland, Ohio, 44135, USA
(216) 433-5919

ABSTRACT

A three–dimensional flow analysis code has been used to compute the design speed operating line of a transonic fan rotor, and the results have been compared to experimental data. The code is an explicit finite difference code with an algebraic turbulence model. It is described in detail in the paper. The transonic fan, designated Rotor 67, has been tested experimentally at NASA Lewis Research Center with conventional aerodynamic probes and with laser anemometry, and has been included as one of the AGARD test cases for computation of internal flows. The experimental data are described briefly. Maps of total pressure ratio and adiabatic efficiency versus mass flow have been computed and are compared to the experimental maps, with excelent agreement between the two. Detailed comparisons between calculations and experiment are made at two operating points, one near peak efficiency and the other near stall. Blade–to–blade contour plots are used to show the shock structure. Comparisons of circumferentially–integrated flow quantities downstream of the rotor show spanwise distributions of several aerodynamic parameters. Calculated Mach number distributions are compared to laser anemometer data within the blade row and the wake to quantify the accuracy of the calculations. Finally, particle traces are used to illustrate the nature of the secondary flow in this fan.

INTRODUCTION

One goal of computational fluid dynamics (CFD) for turbomachinery is the prediction of component performance, for example pressure ratio and efficiency. Since a small improvement in engine efficiency can amount to huge savings in yearly fuel costs for a fleet of commercial aircraft, turbomachinery designers are extremely interested in tools that give good quantitative predictions of turbomachinery performance.

However most of the CFD results for turbomachinery published more than a few years ago show only qualitative comparisons with experimental Mach contours, or quantitative comparisons with surface pressures. This is not to diminish the importance of these results; in the hands of a good turbomachinery designer a shock location or surface pressure distribution can be extremely useful. However CFD for turbomachinery has evolved to a point where it can now provide the designer with reasonable predictions of overall performance of isolated blade rows.

In more recent literature several researchers have presented more detailed predictions of turbomachinery performance. Davis et al. [1] predicted loss buckets for 2D transonic compressor cascades. Chevrin and Vuillez [2] have predicted loss and exit flow angle for turbine and fan cascades using the 2D code of Cambier et al. [3]. Boyle [4] investigated effects of turbulence modelling on turbine blade heat transfer predictions using the 2D code of Chima [5]. In 3D, Pierzga and Wood [6] predicted the static pressure ratio versus mass flow curve of a transonic fan using Denton's code [7], and Dawes [8] has predicted exit total pressure and temperature distributions in a multistage turbine. Adamczyk, et al. [9] investigated the effects of tip clearance on stall for the fan considered in the present work, and predicted pressure ratios and efficiencies for that fan. In [10] Chima used the present code to predict the overall efficiency of an annular turbine stator.

There are many reasons for the scarcity of turbomachinery performance calculations in the early literature. One reason is that pressure field calculations are relatively independent of viscous effects and can be calculated with simple models. Conversely, efficiency and loss calculations are highly dependent on viscous effects and require careful attention to the viscous terms, turbulence modeling, artificial viscosity, and grid resolution for successful calculation. Secondly, computers capable of performing large viscous flow calculations have become generally available only recently. A final reason is that detailed experimental data is difficult to obtain in turbomachinery due to the small size and high speeds of the components involved. Experimental surface pressures are available from many linear and annular cascade tests, which may account for many of the comparisons appearing in the literature. However wake surveys and loss data are often available for the same tests, but tend to be overlooked.

With the publication of AGARD Advisory Report No. 275, *Test Cases for Computation of Internal Flows* *in Aero Engine Components* [11], researchers now have access to some excellent data for the validation of CFD codes for turbomachinery.

In the present work the experimental data described by Strazisar, et al. in [12] and by Wood, et.al. in [11, pp. 165–213] was used to validate the 3D Navier–Stokes code first referenced by Chima and Yokota in [10]. The code, RVC3D (Rotor Viscous Code 3-D), is described, with emphasis on the boundary conditions and artificial viscosity. A new 3D grid code for turbomachinery is also introduced. The test case, a transonic fan rotor (Rotor 67, shown in Fig. 1) is described briefly.

Several operating points were computed along the 100 percent speed line of the rotor. The computed operating curves of adiabatic efficiency and total pressure ratio versus mass flow are compared to the experimental data. Two operating points are examined in detail: one near peak efficiency and one near stall. At each point qualitative comparisons are made between computed and experimental Mach number contours. Comparisons are then made with laser anemometer measurements within the blade row and across the wake, and with conventional aerodynamic measurements downstream. Finally, particle traces are used to illustrate the nature of the secondary flows in this machine.

GOVERNING EQUATIONS

The Navier-Stokes equations are written in a Cartesian (x, y, z) coordinate system rotating with angular velocity Ω about the x-axis. The rotation introduces source terms in the y- and z- momentum equations. The Cartesian equations are mapped to a general body-fitted (ξ, η, ζ) coordinate system using standard techniques. A C-type grid was used in the present work, with the ξ-coordinate roughly following the flow, the η-coordinate running blade-to-blade, and the ζ-coordinate running spanwise. The thin-layer approximation is used to drop all viscous derivatives in the ξ-direction. All viscous terms in the cross-channel (η, ζ) plane are retained. The resulting equations are as follows:

$$\partial_t q + J[\partial_\xi \hat{E} + \partial_\eta \hat{F} + \partial_\zeta \hat{G} - Re^{-1}(\partial_\eta \hat{F}_V + \partial_\zeta \hat{G}_V)] = H \tag{1}$$

where:

$$\hat{q} = J^{-1} \begin{bmatrix} \rho \\ \rho u \\ \rho v \\ \rho w \\ e \end{bmatrix} \quad \hat{E} = J^{-1} \begin{bmatrix} \rho U' \\ \rho u U' + \xi_x p \\ \rho v U' + \xi_y p \\ \rho w U' + \xi_z p \\ e U' + p U \end{bmatrix}$$

$$H = \Omega \begin{bmatrix} 0 \\ 0 \\ -\rho w \\ \rho v \\ 0 \end{bmatrix} \quad \hat{F} = J^{-1} \begin{bmatrix} \rho V' \\ \rho u V' + \eta_x p \\ \rho v V' + \eta_y p \\ \rho w V' + \eta_z p \\ e V' + p V \end{bmatrix}$$

$$\hat{G} = J^{-1} \begin{bmatrix} \rho W' \\ \rho u W' + \zeta_x p \\ \rho v W' + \zeta_y p \\ \rho w W' + \zeta_z p \\ e W' + p W \end{bmatrix} \tag{2}$$

Again, these equations are written in a rotating Cartesian coordinate system attached to the moving blade The code solves for the ***absolute*** velocity components u, v, and w, which point in the x, y, and z coordinate directions, respectively. The *relative* velocity components u', v', and w' are defined with respect to the same rotating coordinate system by subtracting the appropriate components of the blade speed from the absolute velocities, giving:

$$\begin{aligned} u' &= u \\ v' &= v - \Omega z \\ w' &= w + \Omega y \end{aligned} \tag{3}$$

The relative contravariant velocity components are given by:

$$\begin{aligned} U' &= \xi_x u + \xi_y v' + \xi_z w' \\ V' &= \eta_x u + \eta_y v' + \eta_z w' \\ W' &= \zeta_x u + \zeta_y v' + \zeta_z w' \end{aligned} \tag{4}$$

Note that although $u' = u$, $U' \neq U$.

The energy and static pressure are given by:

$$e = \rho \left[C_v T + \frac{1}{2}(u^2 + v^2 + w^2) \right] \tag{5}$$

$$p = (\gamma - 1) \left[e - \frac{1}{2}\rho(u^2 + v^2 + w^2) \right] \tag{6}$$

Using Stokes' hypothesis, $\lambda = -\frac{2}{3}\mu$, the viscous flux $\hat{F}_V$ can be written as follows:

$$\hat{F}_V = J^{-1}\mu [0,\ F_2,\ F_3,\ F_4,\ F_5]^T \tag{7}$$

where

$$\begin{aligned} F_2 &= C_1 \partial_\eta u + C_2 \eta_x + C_3 \partial_\zeta u - C_4 \eta_x + C_5 \zeta_x \\ F_3 &= C_1 \partial_\eta v + C_2 \eta_y + C_3 \partial_\zeta v - C_4 \eta_y + C_5 \zeta_y \\ F_4 &= C_1 \partial_\eta w + C_2 \eta_z + C_3 \partial_\zeta w - C_4 \eta_z + C_5 \zeta_z \\ F_5 &= \frac{\mu \gamma}{Pr}(C_1 \partial_\eta (C_v T) + C_3 \partial_\zeta (C_v T)) \\ &\quad + u F_2 + v F_3 + w F_4 \end{aligned} \tag{8}$$

and

$$\begin{aligned} C_1 &= \eta_x^2 + \eta_y^2 + \eta_z^2 \\ C_2 &= \frac{1}{3}(\eta_x \partial_\eta u + \eta_y \partial_\eta v + \eta_z \partial_\eta w) \\ C_3 &= \eta_x \zeta_x + \eta_y \zeta_y + \eta_z \zeta_z \\ C_4 &= \frac{2}{3}(\zeta_x \partial_\zeta u + \zeta_y \partial_\zeta v + \zeta_z \partial_\zeta w) \\ C_5 &= \eta_x \partial_\zeta u + \eta_y \partial_\zeta v + \eta_z \partial_\zeta w \end{aligned} \tag{9}$$

Terms multiplied by C_1 and C_2 lead to non-mixed second derivative viscous terms like $u_{\eta\eta}$, while terms multiplied by C_3–C_5 lead to mixed-derivative terms like $u_{\eta\zeta}$. The viscous flux vector $\hat{G}$ can be written similarly by interchanging directions η and ζ and replacing F with G everywhere.

Metric terms are defined using the following relations:

$$\begin{bmatrix} \xi_x & \eta_x & \zeta_z \\ \xi_y & \eta_y & \zeta_y \\ \xi_z & \eta_z & \zeta_z \end{bmatrix} = J \begin{bmatrix} y_\eta z_\zeta - y_\zeta z_\eta & y_\zeta z_\xi - y_\xi z_\zeta & y_\xi z_\eta - y_\eta z_\xi \\ x_\zeta z_\eta - x_\eta z_\zeta & x_\xi z_\zeta - x_\zeta z_\xi & x_\eta z_\xi - x_\xi z_\eta \\ x_\eta y_\zeta - x_\zeta y_\eta & x_\zeta y_\xi - x_\xi y_\zeta & x_\xi y_\eta - x_\eta y_\xi \end{bmatrix} \tag{10}$$

where:

$$\begin{aligned} J = \; & (x_\xi y_\eta z_\zeta + x_\zeta y_\xi z_\eta + x_\eta y_\zeta z_\xi \\ & -x_\xi y_\zeta z_\eta - x_\eta y_\xi z_\zeta - x_\zeta y_\eta z_\xi)^{-1} \end{aligned} \tag{11}$$

Terms like x_ξ, x_η, etc. are found using second order central differences. The Jacobian is computed using (11) and stored for the entire grid. All other metric terms are computed as needed using (10.)

The equations are nondimensionalized by arbitrary reference quantities (here the inlet total density ρ_{0ref} and the total sonic velocity c_{0ref} were used,) and the Reynolds number Re and Prandtl number Pr are defined in terms of these quantities. The equations assume that the specific heats C_p and C_v and Prandtl number are constant, that Stoke's hypothesis is valid, and that the effective viscosity for turbulent flows may be written as

$$\mu_{eff} = \mu_{lam} + \mu_{turb} \tag{12}$$

where the laminar viscosity is calculated using a power law function of temperature:

$$\frac{\mu_{lam}}{\mu_{ref}} = \left(\frac{T}{T_{ref}}\right)^n \tag{13}$$

with $n = 2/3$ for air.

The turbulent viscosity μ_{turb} is computed using an adaptation of the Baldwin-Lomax turbulence model [13] on cross-channel planes. Briefly, the model is applied independently in the blade-to-blade and spanwise directions, and the resulting turbulent viscosities are added vectorally. The 2D Buleev length scale based on the distance from the hub and blade is used. The vorticity is calculated in the absolute frame, but the wall shear and wake velocities are calculated in the relative frame. See [10] for details on the 3-D implementation.

BOUNDARY CONDITIONS

Many boundary conditions for turbomachinery are best expressed in cylindrical coordinates, but the code is formulated in Cartesian coordinates. For the boundary conditions, coordinate systems are transformed as needed using:

$$\begin{aligned} v &= (v_r y + v_\theta z)/r \\ w &= (v_r z - v_\theta y)/r \\ v_r &= (vy + wz)/r \\ v_\theta &= (vz - wy)/r \\ r &= \sqrt{y^2 + z^2} \end{aligned} \tag{14}$$

At the inflow boundary the total temperature, total pressure, whirl, and meridional flow angle were specified, and the upstream-running Riemann invariant was extrapolated from the interior. The inlet total temperature T_0 was specified as a constant (standard conditions). The inlet total pressure was specified as a constant in the core flow (also standard conditions) and reduced in the endwall regions according to a 1/7 power law velocity profile, with the inlet boundary layer heights estimated from the experimental data to be 12 mm on both the hub and the casing. At the inlet v_θ was set to zero, and v_r was chosen to make the flow tangent to the meridional projection of the inlet grid lines. The upstream-running Riemann invariant R^- based on the total absolute velocity $Q = \sqrt{u^2 + v^2 + w^2}$ was calculated at the first interior point and extrapolated to the inlet. The Riemann invariant is given by:

$$R^- = Q - \frac{2c}{\gamma - 1} \tag{15}$$

The total velocity is found from T_0 and R^- using:

$$Q = \frac{(\gamma - 1)R^- + \sqrt{2(1-\gamma)(R^-)^2 + 4(\gamma + 1)C_p T_0}}{\gamma + 1} \tag{16}$$

The velocity components are then decoupled algebraically, and the density is found from P_0, T_0, and Q using an isentropic relation.

At the exit the hub static pressure is specified and $\rho, \rho u, \rho v$, and ρw are extrapolated from the interior. The local static pressure is found by integrating the axisymmetric radial equilibrium equation:

$$\frac{dp}{dr} = \frac{\rho {v_\theta}^2}{r} = \frac{\rho}{r^3}(vz - wy)^2 \tag{17}$$

A periodic C–grid was used in the present work. The periodic boundary was solved by setting periodic flow conditions (in terms of cylindrical velocity components) on a dummy grid line outside the boundary. Fourth-difference artificial dissipation terms are neglected on the outer boundary so that only one dummy grid line is needed.

On the blade surface and the rotating part of the hub, $U' = V' = W' = 0$. The hub was specified to be stationary 13.4 mm upstream of the leading edge and 3.35 mm downstream of the trailing edge by setting

$u = v = w = 0$. The tip casing was assumed to be stationary, that is, the blade was assumed to scrape along the casing with zero tip clearance.

Surface pressures were found from the normal momentum equation. On the hub ($\zeta = 1$) and tip ($\zeta = \zeta_{max}$):

$$(\zeta_x\xi_x + \zeta_y\xi_y + \zeta_z\xi_z)\partial_\xi p + (\zeta_x\eta_x + \zeta_y\eta_y + \zeta_z\eta_z)\partial_\eta p + (\zeta_x^2 + \zeta_y^2 + \zeta_z^2)\partial_\zeta p = -\rho[\Omega(\zeta_y w - \zeta_z v)] \qquad (18)$$

On the blades ($\eta = 1$) the normal momentum equation can be found by replacing ζ with η everywhere in (18.) Surface temperatures were found from an adiabatic wall condition implemented as in (18) with p replaced by T and a right–hand side of zero.

MULTISTAGE RUNGE-KUTTA SCHEME

The governing equations are discretized using a node-centered finite difference scheme. Second–order central differences are used throughout.

The multistage Runge-Kutta scheme developed by Jameson, Schmidt, and Turkel [14] is used to advance the flow equations in time from an initial guess to a steady state. If (1) is rewritten as:

$$\partial_t q = -J\left[R_I - (R_V + D)\right] \qquad (19)$$

where R_I is the inviscid residual including the source term, R_V is the viscous residual, and D is an artificial dissipation term described in the next section, then the multistage Runge-Kutta algorithm can be written as follows:

$$\begin{aligned} q_0 &= q_n \\ q_1 &= q_0 - \alpha_1 J\Delta t\left[R_I\, q_0 - (R_V + D)\, q_0\right] \\ &\ \vdots \\ q_k &= q_0 - R_k \\ &= q_0 - \alpha_k J\Delta t\left[R_I\, q_{k-1} - (R_V + D)\, q_0\right] \\ q_{n+1} &= q_k \end{aligned} \qquad (20)$$

Here a standard four-stage scheme was used, with $\alpha_i = 1/4,\ 1/3,\ 1/2,\ 1$. For efficiency both the physical and artificial dissipation terms are calculated only at the first stage, then are held constant for subsequent stages.

ARTIFICIAL DISSIPATION

The dissipative term D in (19) is similar to that used by Jameson et. al. [14]. It is given by:

$$Dq = (D_\xi + D_\eta + D_\zeta)\, q \qquad (21)$$

where the ξ-direction operator is given by

$$D_\xi q = C_\xi\left(V_2 q_{\xi\xi} - V_4 q_{\xi\xi\xi\xi}\right) \qquad (22)$$

The terms V_2 and V_4 are given by:

$$\begin{aligned} V_2 &= \mu_1 + \mu_2 \max\left(\nu_{i+1}, \nu_i, \nu_{i-1}\right) \\ V_4 &= \max\left(0, \mu_4 - V_2\right) \end{aligned} \qquad (23)$$

where:

$$\nu_i = \frac{|P_{i+1} - 2P_i + P_{i-1}|}{min(P_{in}, |P_{i+1} + 2P_i + P_{i-1}|)} \qquad (24$$

and subscript i corresponds to the ξ direction, etc. The constant μ_1 scales a first–order artificial visco ity that is useful for maintaining stability at startu The constant μ_2 scales a first–order artificial artificial viscosity that is switched on at shocks detected b (24). The denominator in (24) is normally constant a the inlet pressure P_{in}, making the operator roughl symmetric across shocks. The more common tern $|P_{i+1} + 2P_i + P_{i-1}|$ is included to switch on the second difference dissipation when the pressure becomes ver small, usually due to numerical problems. The constant μ_4 scales a uniform third–order artificial viscosity that is switched off at shocks by (23). In this worl μ_1 was set to 1/4 for the first 200 iterations and zer thereafter, $\mu_2 = 1/2$, and $\mu_4 = 1/32$.

C is an arbitrary coefficient that can have a large impact on the stability and accuracy of the solution. Th subscript indicates that C may be different in each direction.

In [10] a directionally homogeneous coefficient wa used for 3D problems. To minimize dissipation in viscous regions C was reduced to zero linearly over sevara grid points near walls. In [5] a directionally biased coefficient was used for 2D problems. The dissipatior was proportional to the grid spacing in each direction thus reducing it across finely–gridded viscous regions This worked well in 2D but did not generalize to 3D. Martinelli and Jameson [15] proposed a directionall biased coefficient that works well but can still have large directional variations on highly stretched 3D grids. Kunz and Lakshminarayana [16] proposed modified form of the Martinelli and Jameson coefficient:

$$\begin{aligned} C_\xi &= \frac{1}{J\Delta t_\xi}\left(1 + \frac{\Delta t_\xi}{\Delta t_\eta} + \frac{\Delta t_\xi}{\Delta t_\zeta}\right)^\sigma \\ C_\eta &= \frac{1}{J\Delta t_\eta}\left(1 + \frac{\Delta t_\eta}{\Delta t_\xi} + \frac{\Delta t_\eta}{\Delta t_\zeta}\right)^\sigma \end{aligned} \qquad (25)$$

etc., where $\sigma = 2/3$.

In the present work the 1D time step is approximated as a length scale over a velocity scale. In general the length scale must vary with grid spacing, but the normalized velocity scale can be approximated as one, giving:

$$\Delta t_\xi = \frac{\Delta s_\xi}{V_\xi} \approx \Delta s_\xi \qquad (26)$$

Dissipation coefficients given by (25,26) seem to give a very good distribution of the dissipative terms in each direction, and have been used throughout this work.

THREE-DIMENSIONAL STABILITY LIMIT

The following expression is used for the time step:

$$\Delta t \leq \frac{\lambda^*}{l_x|u| + l_y|v'| + l_z|w'| + \sqrt{c^2(l_x^2 + l_y^2 + l_z^2) + \Omega^2}}$$

where:

$$\begin{aligned} l_x &= |\xi_x| + |\eta_x| + |\zeta_x| \\ l_y &= |\xi_y| + |\eta_y| + |\zeta_y| \\ l_z &= |\xi_z| + |\eta_z| + |\zeta_z| \end{aligned} \qquad (27)$$

and λ^* is the maximum Courant number for the particular multistage scheme. For the standard four-stage scheme $\lambda^* \approx 2.8$.

To accelerate convergence to a steady state the maximum permissible time step at each grid point was used giving a constant Courant number everywhere. The time step was updated every 50 iterations.

IMPLICIT RESIDUAL SMOOTHING

To further accelerate convergence it is desirable to use a time step even larger than the stability limit given by (27). To maintain stability, the residual calculated in (19) is smoothed after each Runge-Kutta stage by an implicit smoothing operator, i.e.,

$$(1 - \epsilon_\xi \delta_{\xi\xi})(1 - \epsilon_\eta \delta_{\eta\eta})(1 - \epsilon_\zeta \delta_{\zeta\zeta})\bar{R}_k = R_k \qquad (28)$$

where $\delta_{\xi\xi}$, $\delta_{\eta\eta}$, and $\delta_{\zeta\zeta}$ are standard second difference operators and ϵ_ξ, ϵ_η, and ϵ_ζ are smoothing parameters. Linear stability analysis shows that the Runge-Kutta scheme may be made unconditionally stable using implicit residual smoothing if the smoothing parameters ϵ are made sufficiently large [17]. In one dimension:

$$\epsilon \geq \frac{1}{4}\left[\left(\frac{\lambda}{\lambda^*}\right)^2 - 1\right] \qquad (29)$$

gives unconditional stability if λ^* is the Courant limit of the unsmoothed scheme, and λ is a larger operating Courant number. In three dimensions different ϵ's may be used in each direction, and their magnitudes may often be reduced below the value given by (29). Courant numbers $\lambda^* \approx 2.8$, $\lambda = 5.0$, and smoothing parameters $\epsilon_\xi = 0.4$, $\epsilon_\eta = 0.55$, and $\epsilon_\zeta = 0.45$ were used in the present work.

COMPUTATIONAL GRID

A three-dimensional grid code for turbomachinery has been developed by the author (currently unpublished.) The code, called TCGRID for Turbomachinery C-GRID, generates three-dimensional C-type grids using the following technique:

1. A coarse, equally-spaced meridional grid is generated between the specified hub and tip.
2. Blade coordinates are found at the meridional grid points by interpolation of the input blade geometry.
3. Two-dimensional blade-to-blade grids are generated along the meridional grid lines in $(m, \bar{r}\theta)$ coordinates using a version of the GRAPE code developed by Steger and Sorenson [18]. Here m is the arc length along the meridional surface, and $\bar{r}$ is some mean radius. The GRAPE code allows arbitrary specification of inner and outer boundary points, then generates interior points as the solution of a Poisson equation. Forcing terms in the Poisson equation are chosen to maintain the desired grid spacing and angles at the boundaries.
4. The $(m, \bar{r}\theta)$ coordinates are transformed back to (z, r, θ).
5. The two-dimensional grids are reclustered spanwise using a hyperbolic tangent stretching function to make a full three-dimensional grid.
6. Finally the (z, r, θ) coordinates are transformed to (x, y, z) and stored in a standard format.

Figure 2 shows the 185x40x49 grid used for Rotor 67. The C-shaped grids used here give good resolution of the round leading edge of the blade, as shown in Fig. 3. The initial grid spacing is about 0.015 mm at the blade, 0.03 mm at the hub, and 0.045 mm at the tip.

COMPUTATIONAL DETAILS

All computations were run on the Cray Y-MP computer at NASA Ames Research Center, under support from the Numerical Aerodynamic Simulation (NAS) Project Office.

The grid code required about 3 million words (Mw) of in-core storage and ran in about 15 seconds for the grid shown in Figs. 2 and 3 (362 600 points.) The flow solver required about 6.5 Mw of storage and 3.6 Mw of solid state device storage (SSD.) The SSD storage is used to hold the old solution q_0 and the dissipative terms $R_V + D$ during the four stages of the multistage scheme (20.)

The spanwise inlet profile was used as an initial guess, and 250 iterations were run with an exit pressure corresponding to the peak efficiency point. About 20 minutes of CPU time were required for this startup solution. All subsequent calculations were restarted from this solution and run an additional 1550 iterations, requiring about 2.5 CPU hours per case.

EXPERIMENTAL DETAILS

Experimental details are described briefly below. Full details may be found in [11,12].

Test Rotor – The test rotor, NASA designation Rotor 67, is shown in Fig. 1. It is the first-stage rotor of a two-stage fan, with a design pressure ratio of 1.63 at a mass flow of 33.25 kg/sec. The rotor has 22 blades. The tip radius varies from 25.7 cm at the leading edge to 24.25 cm at the trailing edge, and the hub/tip radius ratio varies from 0.375 to 0.478. At the design rotational speed of 16 043 rpm the tip speed is 429 m/sec and the tip relative Mach number is 1.38.

Aerodynamic Performance Measurements – The rotor mass flow was determined using a calibrated orifice. Radial surveys of total pressure and temperature, static pressure, and flow angle were made 2.54 cm upstream of the leading edge and 2.02 cm downstream of the trailing edge using conventional probes.

Laser Anemometry Measurements – A single–channel fringe anemometer was used for the measurements described below. Optical access to the fan was through a glass window in the casing. Fluorescent oil droplets with a diameter of about 1.0–1.4 μm were used to seed the flow.

Measurements were made by holding the probe volume fixed in space as the blades rotated by. Measurement were taken in 50 intervals going from the suction surface of one blade to the suction surface of the next blade. In [11,12], and in the present work the term *windows* is used interchangeably with the term *intervals* in referring to laser measurement locations. Within the blade row the blade itself obscures the last few windows. Measurements were taken in 17 consecutive blade passages, then averaged. Only axial and tangential velocities were measured; however Pierzga and Wood [6] have shown numerically that neglecting the radial component has a minimal effect on calculated Mach numbers.

RESULTS

The computed total pressure ratio and adiabatic efficiency at 100 percent speed are plotted against normalized mass flow and compared to experimental data in Fig. 4. The computed and experimental mass flows are normalized by their respective choking mass flows, as suggested by Pierzga and Wood [6]. This normalization removes any uncertainties in the experimental mass flows. The choking mass flow was measured as 34.96 kg/sec using a calibrated orifice, and the computed value was 34.54 kg/sec, a difference of 1.2 percent. The computed pressure ratios and efficiencies agree very well with the experimental data, except that they are slightly high near stall.

Figures 5–8 show detailed results at an operating point near peak efficiency. Figure 5 shows a comparison of relative Mach number contours at 10, 30, and 70 percent span from the tip. The experimental contours were drawn from laser anemometry data using smoothing and interpolation procedures outlined in [6]. At 10 percent span the inlet Mach number is about 1.35, and a bow wave stands ahead of the blade. A weak oblique shock crosses the passage inside the blade row, and a strong normal shock sits near the trailing edge. The flow exits at a Mach number of about 0.95. The flow is qualitatively similar at 30 percent span, except that the shock sits more forward. At 70 percent span the inlet Mach number is about 0.95. A small supersonic bubble forms on the forward portion of the suction surface. It is not clear if this bubble is terminated by a shock.

Figure 6 shows a comparison of computed and measured blade–to–blade profiles of relative Mach number versus laser window number at two axial locations for each of three spanwise locations. The first axial location is within the blade row and the second is within the wake. Again, 50 laser windows are defined from the suction surface of one blade (window 0) to the suction surface of the next blade (window 50.)

Within the blade row the computed profiles agree reasonably well with the laser data and predict the shock locations accurately. At 70 percent span near the pressure surface (laser windows greater than 40), few seed particles were observed and the data is statistically uncertain.

Within the wake the computed Mach numbers are somewhat low near the tip, and get progressively better towards the hub. The computed wake profiles are deeper than the measured profiles. It is thought tha this is because the seed particles used for the lase anemometer measurements could not follow the high shear rates found at the center and edges of the wake

The computational results were averaged blade–to–blade using a so–called "energy average" procedure developed by D. L. Tweedt at NASA Lewis Reasearch Center (unpublished.) On each blade–to–blade grid line the procedure integrates the mass flow, radial and tangential momentum, total enthalpy, and ideal total enthalpy $P_0^{\frac{\gamma-1}{\gamma}}$. The radial distributions were mass–averaged spanwise to produce the overall averages shown previously in Fig. 4. Since the integrations give total conditions directly, they can be expected to give good predictions of efficiency. Other quantities like average static pressure or flow angle are found as nonlinear algebraic combinations of the primitive integrated quantities, and thus may not agree as well with experimental data.

Experimentally the exit total conditions and flow angle were measured with a self-nulling combination probe, and static pressure was measured using a separate self-nulling wedge probe. Total conditions are thought to be fairly accurate, but flow angle and static pressure accuracy depend on the frequency response and blockage of the instrumentation.

With these thoughts in mind, radial surveys of several aerodynamic parameters measured 2.02 cm downstream of the rotor (at the grid exit) are shown in Fig. 7. The computed exit total temperatures and total pressures agree very well with the measurements along the span, but the computed static pressures are somewhat high, and computed exit flow angles are two to three degrees high over much of the span.

Figure 8 shows several particle traces to illustrate some of the secondary flows in this fan. The overall view shows particles introduced upstream so as to pass over the suction surface of the blade. Most of the particles pass straight through the blade row, but those in the endwall boundary layer roll up into a vortex that climbs the leading edge. The enlargement of the leading edge shows that the flow in the hub boundary layer sees a high blade incidence and separates near the leading edge. The low-momentum fluid in this separated region is centrifuged radially outwards. Eventually the incidence decreases and the flow turns abruptly in the streamwise direction. The trailing edge enlargement shows a large separation bubble fed by fluid from the endwall that migrates radially outward and ends up in the wake. The complicated flow pattern in this region may explain the scarcity of laser seed particles observed in this region.

Figures 9–12 show detailed results at an operating point near stall. Figure 9 shows a comparison of relative Mach number contours, again at 10, 30, and 70 percent span from the tip. At 10 percent span the inlet Mach number is about 1.4. A normal shock stands ahead of the blade and crosses the passage. The computed shock is somewhat stronger than, and ahead of, the measured shock. The exit Mach number is about 0.85. At 30 percent span the results are similar. The flow at 70 percent span is similar to the peak efficiency case, except that the supersonic bubble is smaller and has a better-defined (though smeared) terminating shock.

Figure 10 shows a comparison of relative Mach number profiles, again at two axial locations and three spanwise locations. At the tip the computed shocks are ahead of and stronger than the measured shocks, which accounts for the high predicted pressure ratios near stall. Adamczyk, et al. [9] have shown numerically that interaction of the tip leakage vortex and the tip shock has a large effect on the near–stall performance of this rotor, and that lack of a tip clearance model can account for the discrepancies in shock position and strength seen here. At 70 percent the computed Mach numbers are slightly low, but agree qualitatively with the data.

In the wake, the computed Mach numbers are somewhat low near the tip, and get progressively better towards the hub. Again the computed wakes are deeper than the measured wakes. There is considerable uncertainty in the laser data in the center of the wake at 70 percent span, where computed particle traces shown later indicate a large separation.

Figure 11 compares radial surveys downstream of the rotor. The computed total temperatures and pressures are slightly high along the span, consistent with the high adiabatic efficiency shown in Fig. 4. Again the computed static pressures are high. Computed exit flow angles agree well near the tip but are a few degrees high at lower radii.

Figure 12 shows particle traces at the near–stall operating point. The overall view shows more radial migration of the endwall flow than at peak efficiency. At this lower mass flow the blade sees a higher relative incidence than at peak efficiency, causing the flow near the hub to migrate tangentially away from the suction surface, as shown in the leading edge enlargement. The trailing edge enlargement shows a separation bubble similar to that seen near peak efficiency. The trailing edge separation appears to be slightly larger at the near–stall point.

SUMMARY

A flow analysis code has been developed for 3D viscous flows in turbomachinery. The analysis solves the Navier-Stokes equations written in a general body-fitted coordinate system, including rotation about the x-axis. The thin-layer approximation is made in the streamwise direction but all viscous terms are included in the cross-planes. The Baldwin-Lomax eddy-viscosity model is used for turbulent flows.

An explicit multistage Runge-Kutta scheme is used to solve the finite-difference form of the flow equations. A variable time step and implicit residual smoothing are used to accelerate the convergence of the scheme. The code is highly vectorized for the Cray Y-MP, and solutions can be computed on fairly fine grids in two to three hours.

The code was used to compute the operating map of a transonic fan at design speed, and showed good agreement with measured values of total pressure ratio and adiabatic efficiency. The computed results are slightly optimistic near stall, probably due to the lack of a tip clearance model.

Detailed comparisons were made with experimental data at two operating points, one near peak efficiency and one near stall. Comparisons were made with aerodynamic surveys downstream of the fan. In general, exit total temperature and total pressure were predicted quite accurately, but static pressure and flow angle showed some disagreement with the data. Comparisons were also made with laser anemometry data in the blade row and in the wake. Shock location and strength were predicted closely near peak efficiency, but were over–predicted near stall. Predicted wake profiles had about the right spread, but were off in location in some cases. Predicted wakes were much deeper than measured wakes, probably due to lack of resolution in the laser data.

Particle traces showed separated flow at both the leading and trailing edges at both operating points. The leading edge separation is too small to be seen in the laser data. The trailing edge separation may have been suggested indirectly by the scarcity of seed particles in this region. The ability of the code to predict these separated flow features suggests that the code could be used to guide experimental work aimed at resolving these features, or to eliminate such features during design.

Overall the code showed very good agreement with a variety of experimental data, thereby increasing confidence that the code can reliably be used to predict the performance of other machines as well.

References

[1] Davis, R. L., Hobbs, D. E., Weingold, H . D., "Prediction of Compressor Cascade Preformance Using a Navier–Stokes Technique," ASME Paper 88-GT-96, June, 1986.

[2] Chevrin, P.–A., Vuillez, C., "Viscous Flow Computations in Turbomachine Cascades," ASME Paper 90-GT-76, June, 1990.

[3] Cambier, L., Escande, B., Veuillot, J. P., "Computation of Internal Flows at High Reynolds Number by Numerical Solution of the Navier–Stokes Equations," *Rech. Aérosp.*, No. 1986-6, pp 27–44.

[4] Boyle, R. J., "Navier–Stokes Analysis of Turbine Blade Heat Transfer," ASME Paper 90–GT–42, June, 1990.

[5] Chima, R. V., "Explicit Multigrid Algorithm for Quasi-Three-Dimensional Viscous Flows in Turbomachinery," *J. Propulsion and Power*, Vol. 3, No. 5, Sept.-Oct. 1987, pp. 397–405.

[6] Pierzga, M. J., Wood, J. R., "Investigation of the 3–D Flow Field Within a Transonic Fan Rotor: Experiment and Analysis," *J. Eng. Gas Turbines and Power,* Vol. 107, No. 2, Apr. 1985, pp. 436–449.

[7] Denton, J. D., "An Improved Time Marching Method For Turbomachinery," ASME Paper 82–GT–239, Apr. 1982.

[8] Dawes, W. N., "Towards Improved Throughflow Capability: The Use of Viscous Flow Solvers in a Multistage Environment," ASME Paper 90–GT–18, June, 1990.

[9] Adamczyk, J. J., Celestina, M. L., Greitzer, E. M., "The Role of Tip Clearance in High-Speed Fan Stall," to be presented at the 1991 ASME Gas Turbine Conf., June 3–6, 1991, Orlando, FL.

[10] Chima, R. V., Yokota, J. W., "Numerical Analysis of Three-Dimensional Viscous Internal Flows," AIAA J., Vol. 28, No. 5, May 1990, pp. 798–806.

[11] Fottner, L., ed., *Test Cases for Computation of Internal Flows in Aero Engine Components,* Propulsion and Energetics Panel Working Group 18, AGARD Advisory Report No. 275, July, 1990, Specialised Printing Services Ltd, Essex, U.K.

[12] Strazisar, A. J., Wood, J. R., Hathaway, M. D., Suder, K. L., "Laser Anemometer Measurements in a Transonic Axial Flow Fan Rotor," NASA TP-2879, Nov. 1989.

[13] Baldwin, B. S., Lomax, H., "Thin–Layer Approximation and Algebraic Model for Separated Turbulent Flows," AIAA Paper 78-257, Jan. 1978.

[14] Jameson, A., Schmidt, W., Turkel, E., "Numerical Solutions of the Euler Equations by Finite Volume Methods Using Runge-Kutta Time-Steppin Schemes," AIAA Paper 81-1259, June 1981.

[15] Martinelli, A., Jameson, A., "Validation of Multigrid Method for the Reynolds Average Equations," AIAA Paper 88-0414, Jan. 1988.

[16] Kunz, R., F., Lakshminarayana, B. "Computation of Supersonic and Low Subsonic Cascad Flows Using an Explicit Navier-Stokes Techniqu and the $k - \epsilon$ Turbulence Model," in *Computational Fluid Dynamics Symposium on Aeropropulsion*, NASA Conference Publication 10045, Apr 24-26, 1990.

[17] Jameson, A., Baker, T. J., "Solution of the Eule Equations for Complex Configurations," AIA Paper 83-1929, July 1983.

[18] Steger, J. L., Sorenson, R. L., "Automatic Mesh-Point Clustering Near a Boundary in Grid Generation with Elliptic Partial Differential Equations," *Journal of Computational Physics*, Vol 33, No. 3, Dec. 1979, pp. 405-410.

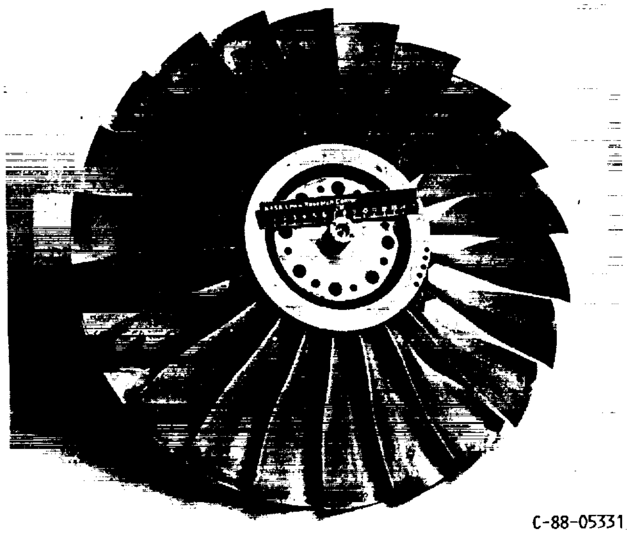

C-88-05331

Figure 1. Rotor 67 test hardware.

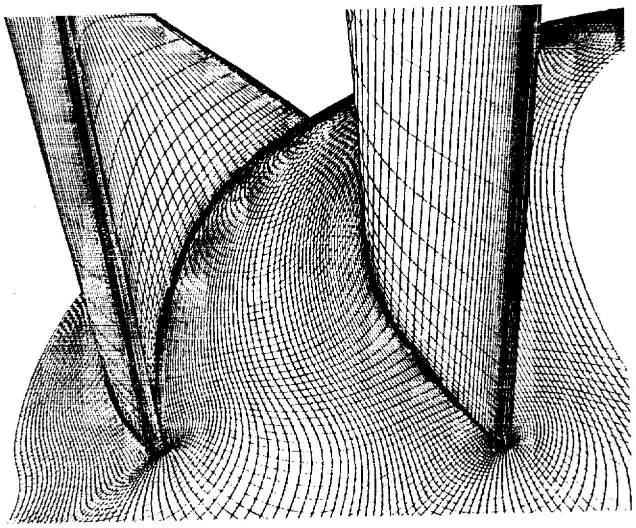

Figure 3. Grid leading edge enlargement.

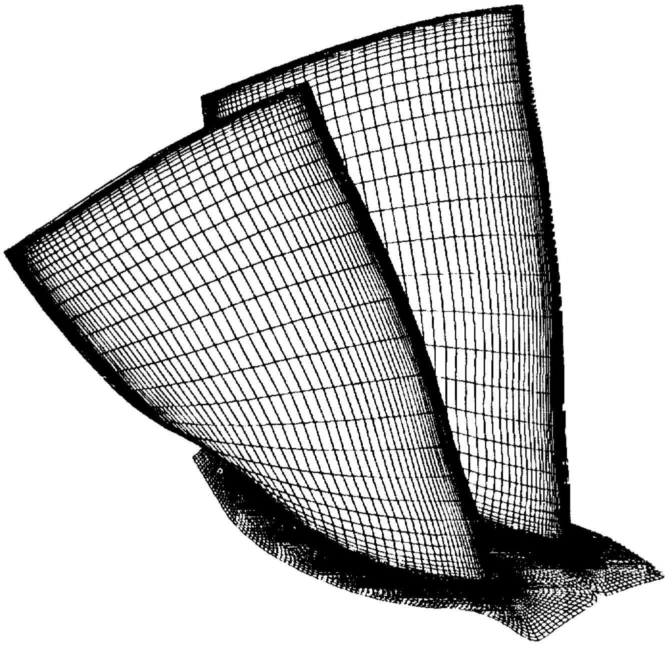

Figure 2. Computational grid.
185 C x 40 tangential x 49 spanwise points.

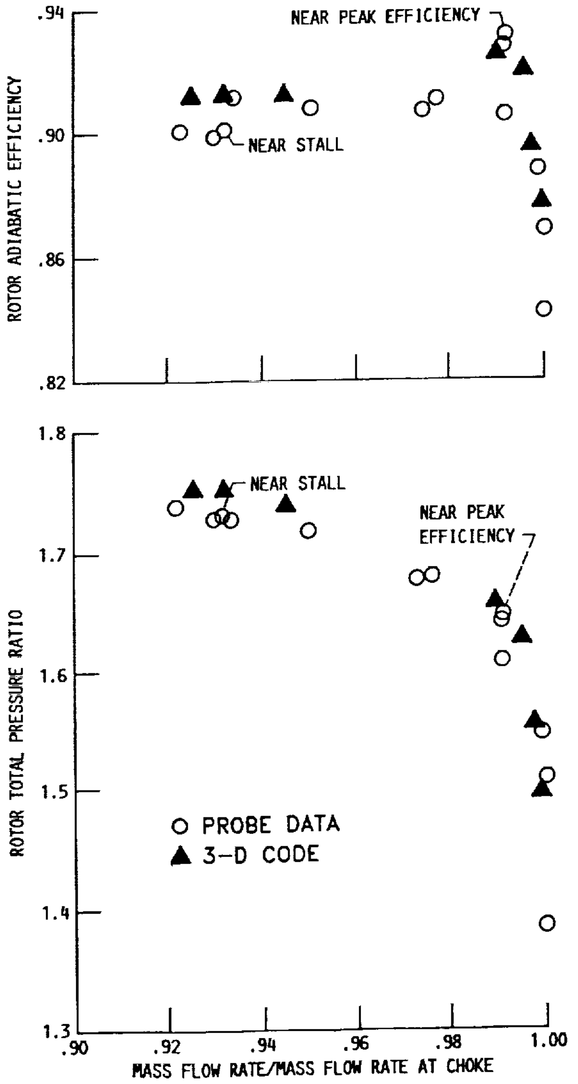

Figure 4. Comparison of computed and measured adiabatic efficiency and total pressure ratio characteristic at 100 percent speed. Points labelled “NEAR STALL” and “NEAR PEAK EFFICIENCY” are discussed in detail in the text.

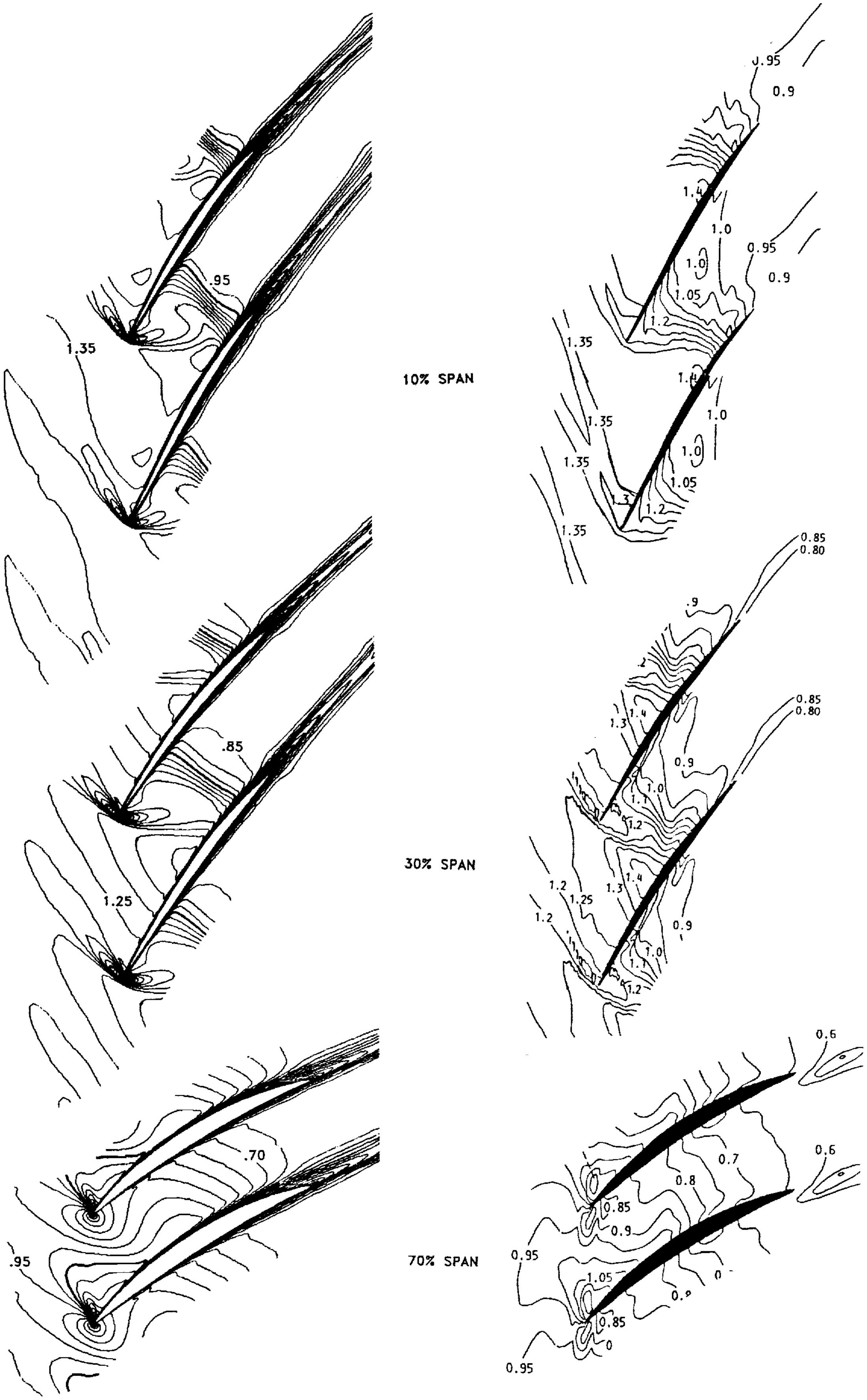

Figure 5. Computed contours of relative Mach number, near peak efficiency. Heavy line is $M = 1.0$, contour increment $= 0.05$.

Measured contours of relative Mach number, near peak efficiency.

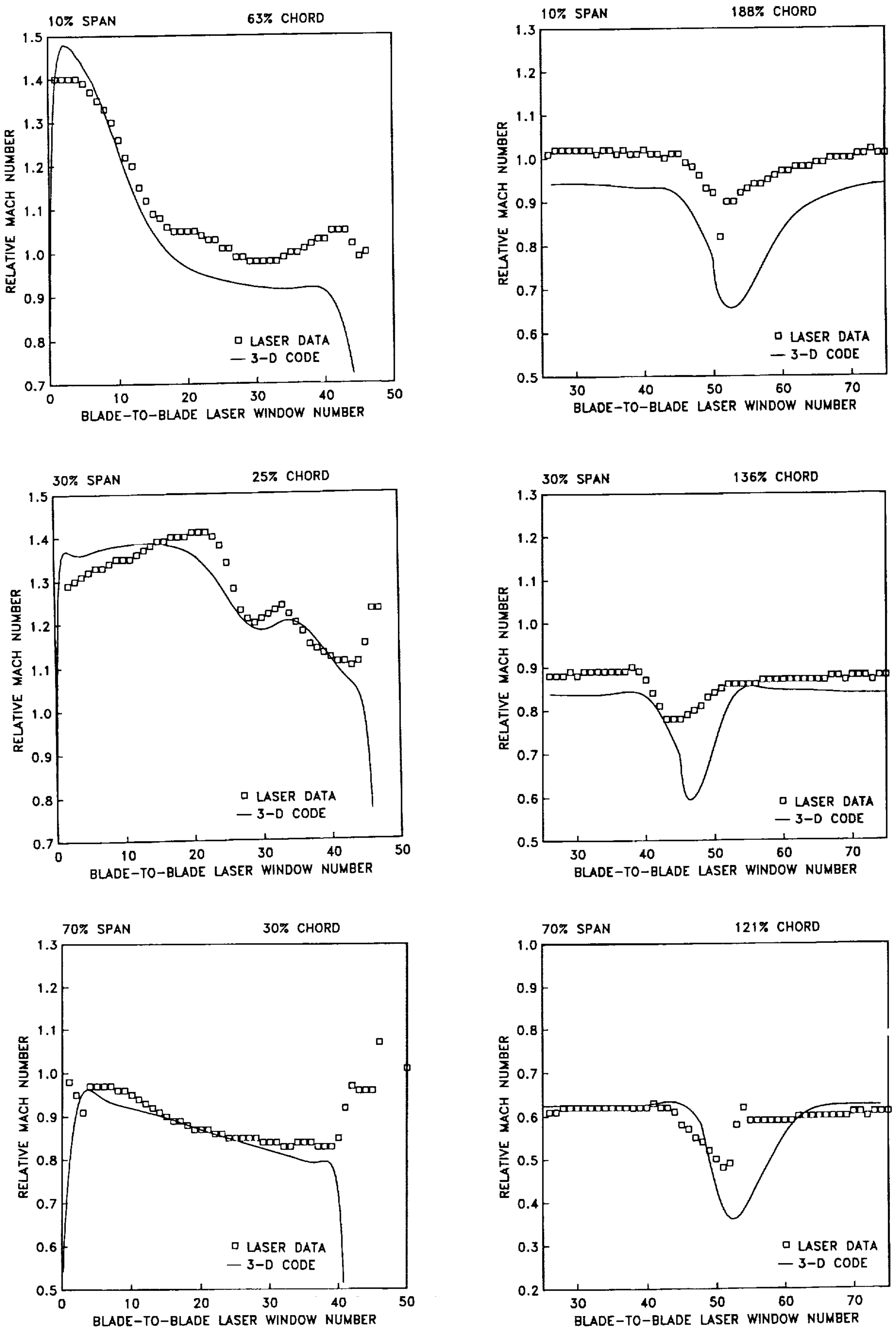

Figure 6. Comparison of computed and measured blade-to-blade distributions of relative Mach number, near peak efficiency.

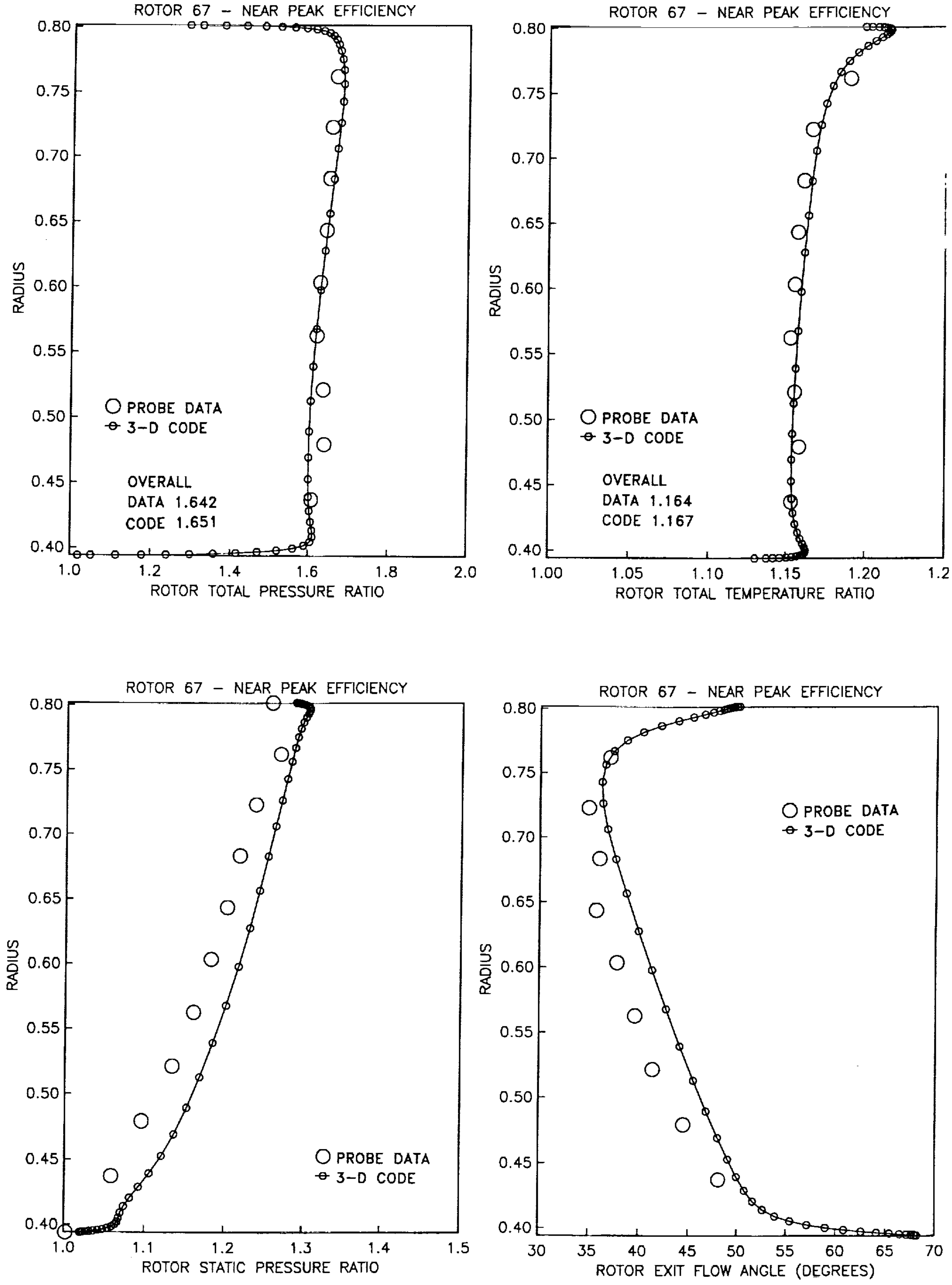

Figure 7. Comparison of computed and measured spanwise distributions of total pressure, total temperature, static pressure, and flow angle downstream of the rotor, near peak efficiency.

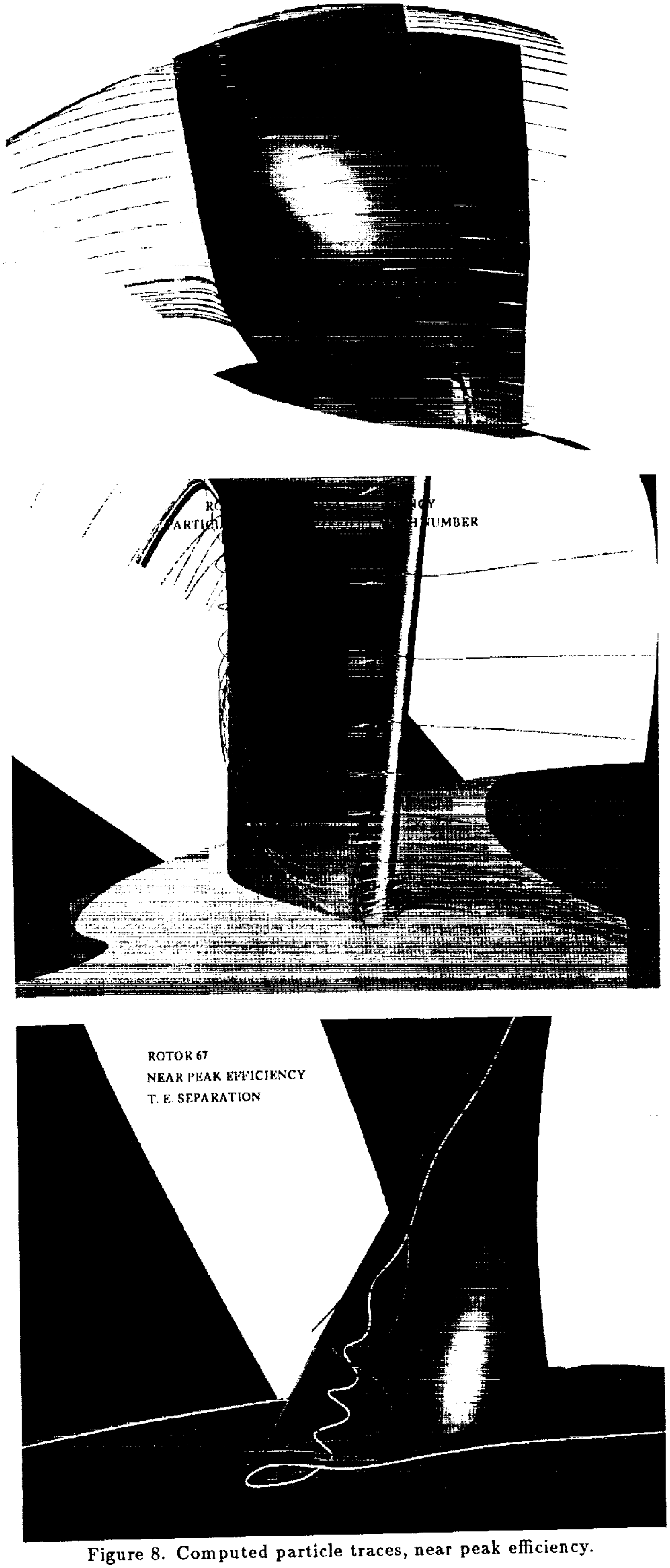
ROTOR 67
NEAR PEAK EFFICIENCY
T. E. SEPARATION

Figure 8. Computed particle traces, near peak efficiency.
Top: Suction surface overview.
Center: Leading edge enlargement looking downstream.
Bottom: Trailing edge enlargement looking upstream.

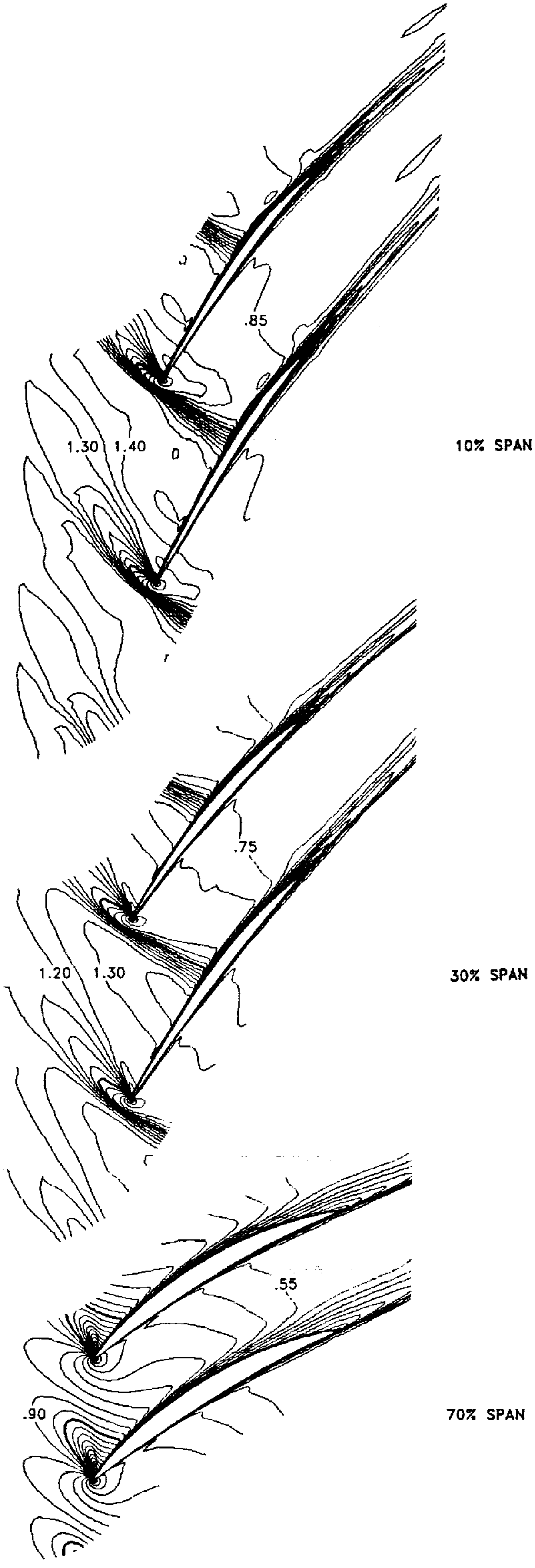

Figure 9. Computed contours of relative Mach number, near stall. Heavy line is $M = 1.0$, contour increment = 0.05.

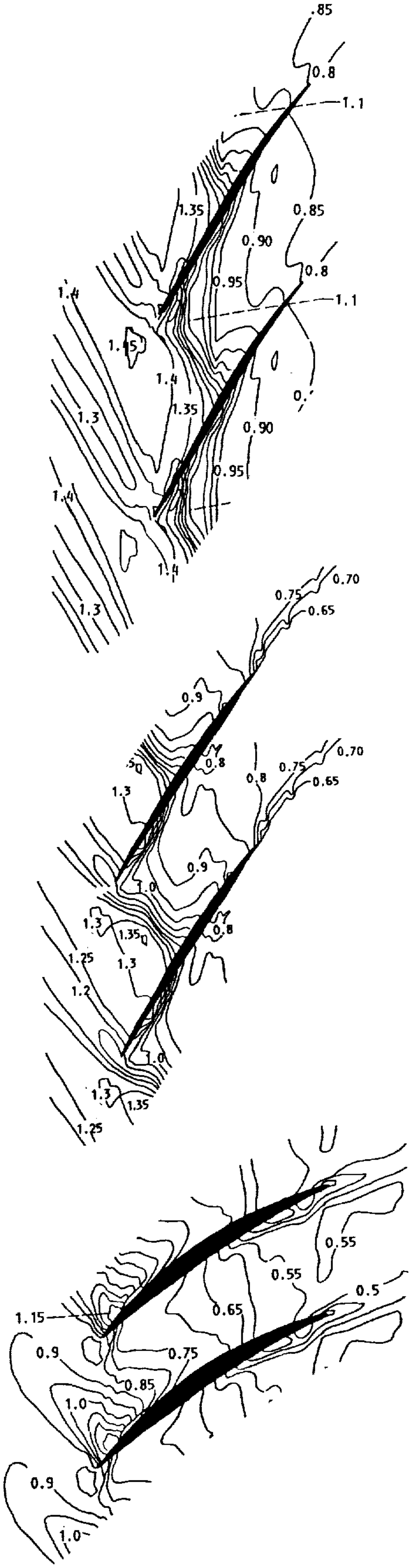

Measured contours of relative Mach number, near stall.

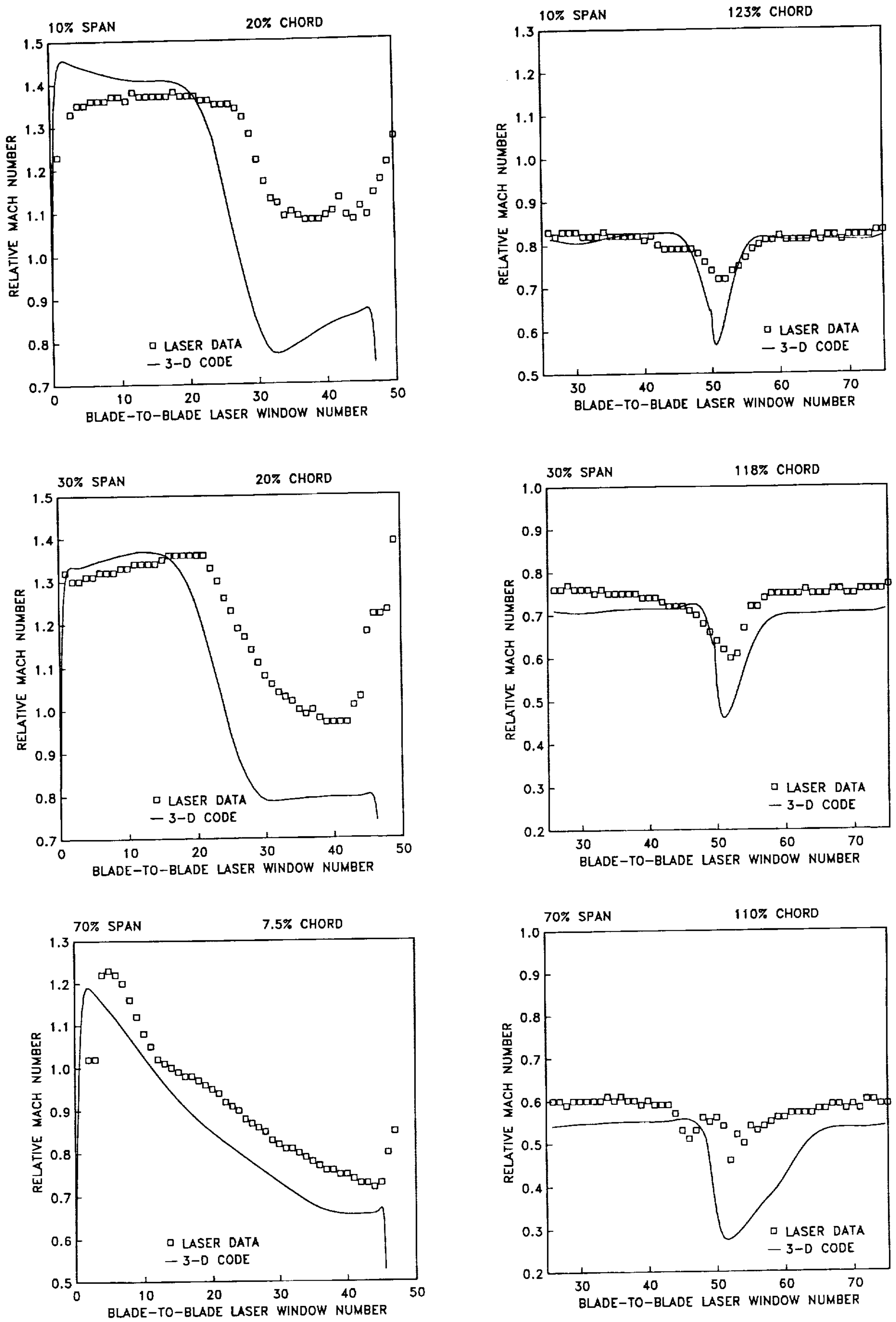

Figure 10. Comparison of computed and measured blade-to-blade distributions of relative Mach number, near stall.

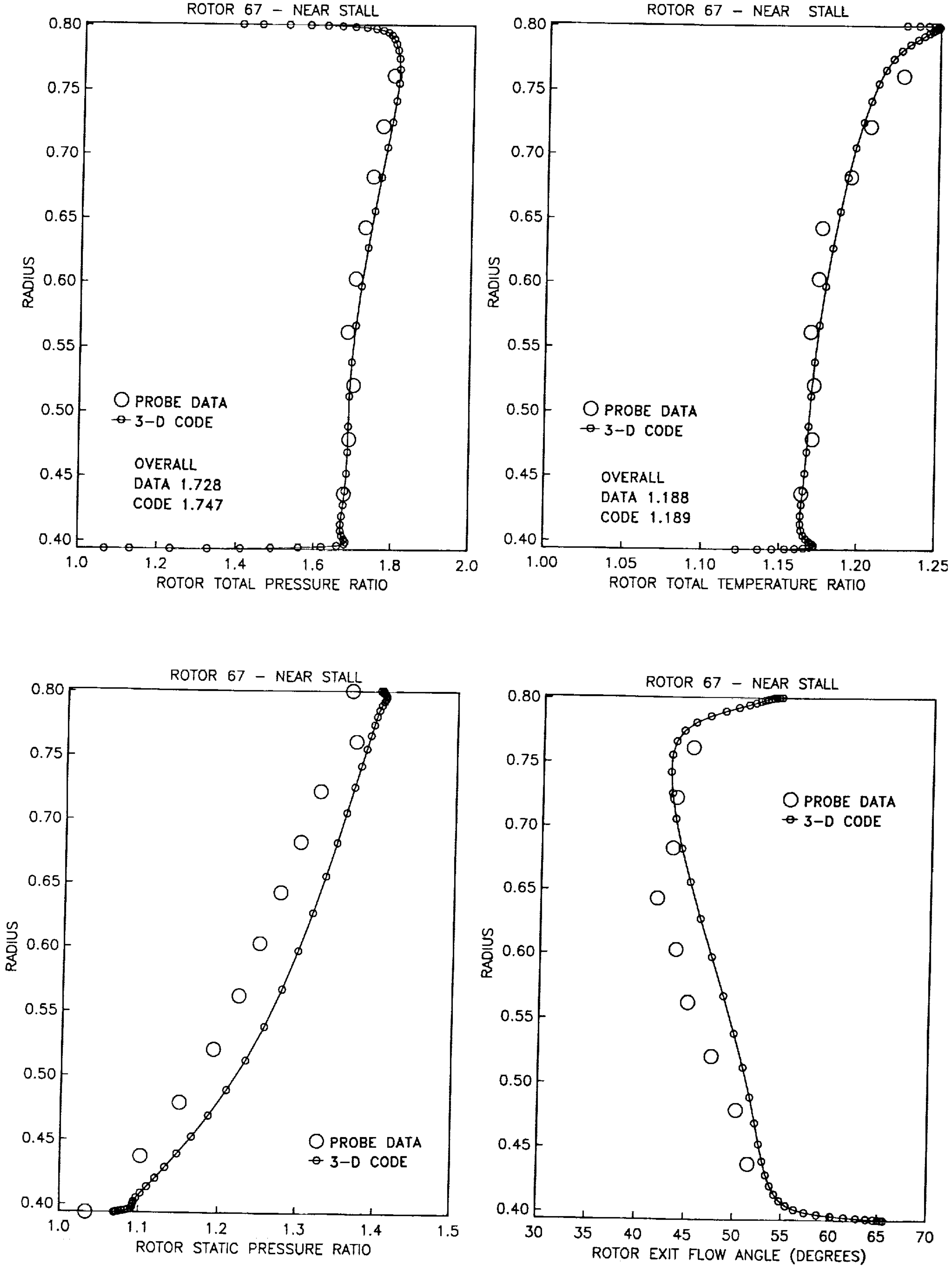

Figure 11. Comparison of computed and measured spanwise distributions of total pressure, total temperature, static pressure, and flow angle downstream of the rotor, near stall.

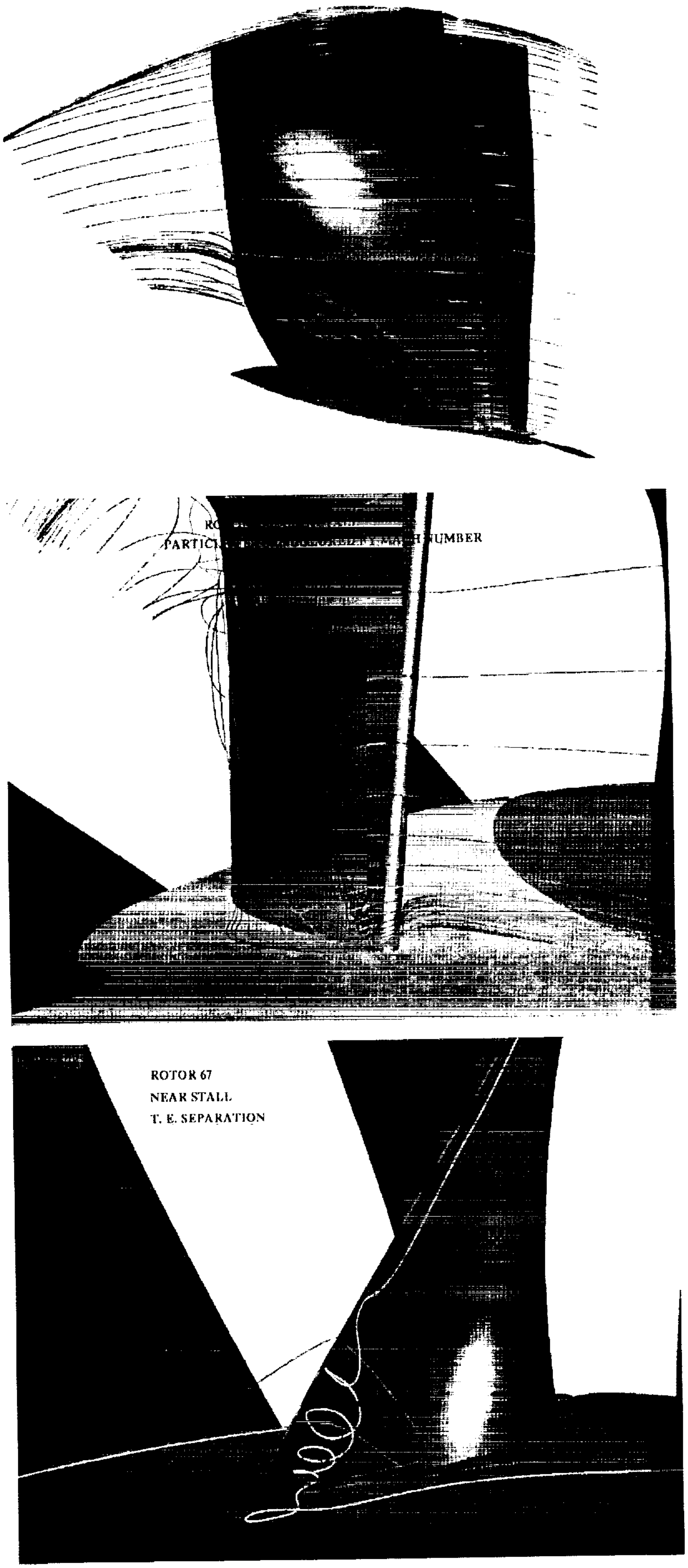
ROTOR 67
NEAR STALL
T. E. SEPARATION

Figure 12. Computed particle traces, near stall.
Top: Suction surface overview.
Center: Leading edge enlargement looking downstream.
Bottom: Trailing edge enlargement looking upstream.

Discussion

T. PRINCE, WILLIAMS INTER., U.S.A.

Have you investigated the hysteresis effect, where Rotor 67 exhibits two distinct levels of performance at the peak efficiency point?

AUTHOR'S REPLY

The efficiencies computed when approaching peak efficiency from either side seemed to follow the speculation of the experimentalists. The difference in the computed efficiencies was about half the measured differences. The differences in the flows were hard to detect - slight differences in shock location and strength. I suspect that the hysteresis effect is computable, but will require a very precise and systematic computational study. I also suspect that the final results will not show dramatic differences between the two solutions.

P. RAMETTE, DASSAULT AVIATION, FRANCE

1) What is the extent of the separation zone at the trailing edge near the hub?
2) Did you compute the flow near the tip, taking into account tip clearance effects?

AUTHOR'S REPLY

1) The trailing edge separation covers roughly the last 25 percent chord and the bottom 20 percent span of the blade.

2) There is no tip clearance model in the present code. The blade is assumed to scrape without leakage against a stationary endwall.

W. CALVERT, RAE PYESTOCK, U.K.

1) I notice from your paper that your calculations underestimated the mass flow of this fan by 1.2 percent, which is consistent with the results from my calculations using a S1-S2 system. Can you comment on whether this is a common feature for all CFD predictions carried out on this fan?

2) What transition model is used in your code?

AUTHOR'S REPLY

1) The mass flow for the fan was found experimentally both by use of a calibrated orifice and by integrating measured inlet profiles. The two methods give somewhat different results, but the orifice value is generally taken as correct. My computed choking mass flow differs from the orifice value by 1 to 2 percent (lower than measured). I don't know how close other researchers have come to predicting the choking mass flow. Pierzga and Wood (Ref. 6) have recommended normalizing the computed mass flows at other operating points by the computed choking mass flow in order to minimize uncertainties in the experimental mass flows. That procedure was used for the operating curves shown in Fig. 4.

2) The Baldwin-Lomax turbulence model uses the following transition model: The turbulent viscosity is computed for a given velocity profile. If the maximum value is less than 14 times the laminar viscosity, the flow is assumed to be laminar, and the turbulent viscosity is reset to zero. When the maximum value exceeds 14 times the laminar viscosity, the flow is taken to be turbulent.

C. HIRSCH, UNIV. OF BRUSSELS, BELGIUM

1) What is the CFL number and convergence levels of your computation?

2) Can you comment on the validity of the thin shear layer approximation compared to full Navier-Stokes, taking into account the fact that your results show regions of large three-dimensional separations.

AUTHOR'S REPLY

1) The calculations were all run at a Courant number of 5.0. Each case was run for a total of 1800 iterations, at which point the residuals were reduced about three orders of magnitude. Several other parameters were monitored for convergence. Global mass conservation was generally better than 0.2 percent, and adiabatic efficiency was converged to three decimal places.

2) The thin shear layer approximation neglects all viscous derivatives along streamwise grid lines, based on the fact that the streamwise grid spacing may be several orders of magnitude larger than the spacing across the viscous layer. Even if streamwise viscous terms are included, their effects cannot be resolved on the relatively coarse streamwise grid. Several papers, notably one by Steger, have demonstrated this in the past. Although the thin shear layer approximation superficially resembles the boundary layer approximation, the normal momentum equation is retained, allowing calculation of separated flows.

F. BASSI, UNIV. OF CATANIA, ITALY

Have you tried or do you plan to use a multigrid technique in your code?

AUTHOR'S REPLY

Although I have worked with multigrid in the past, my three-dimensional code does not use multigrid. I may add it in the future.